Phase selection rule of high-entropy metallic glasses with different short-to-medium-range orders

Hui-Qiang Ying, Si-Nan Liu, Zhen-Duo Wu*, Wei-Xia Dong, Jia-Cheng Ge, Horst Hahn, Virgil Provenzano, Xun-Li Wang, Si Lan*

When an equiatomic multi-component alloy is quenched from its molten state down to room temperature, either a solid solution crystalline alloy or a metallic glass is formed. The former is called a high-entropy alloy, whereas the latter is referred as a high-entropy metallic glass (HE-MG). In such multicomponent alloys, thermodynamic parameters, e.g., the mixing entropy, the mixing enthalpy and other parameters such as atomic size mismatch, determine the resulting phases. In this work, we studied the phase selection rule applied to the equiatomic multicomponent $Ti_{20}Zr_{20}Hf_{20}Cu_{20}Ni_{20}$ HE-MG from a structural perspective, by analyzing the short-to-medium-range orders. It was found that the short-range order in this MG resembles a body-centered cube structure, while the medium-range order is comprised of different orders. The experimental data suggest that different packing schemes, at the medium-range scale, play a critical role in the phase selection rule with regard to an amorphous phase or solid solution.

In recent years, equiatomic multicomponent alloys, particularly the high-entropy alloys (HEA), have attracted tremendous research interests because of their remarkable novel mechanical properties [1–10]. However, a limited number of alloy systems form crystalline solid solutions, whereas the rest forms either amorphous [11–17] or intermetallic phases [18, 19]. In order to design alloys with desirable structure and properties, it is important to have an understanding of the phase selection rule, which ultimately determines the phases that will be present. Guo and Liu [20] pointed out that solid solution phases form when atomic size mismatch, mixing enthalpy and mixing entropy all meet specific requirements. Yang and Zhang [21] calculated two parameters, Ω (the entropy of mixing times the average melting temperature of the elements over the enthalpy of mixing) and σ (the mean square deviation of the atomic size of elements), which can be employed to predict the formation of solutions, amorphous or intermetallic phases. Despite the excellent prediction using the above parameters, the underlying structural mechanism of phase selection remains unsolved for equiatomic multicomponent alloys.

High-entropy metallic glass (HE-MG) is an appropriate model system for studying the phase selection rule. In such a system, the liquid structure is retained in the glassy state as it freezes. This opens an opportunity for understanding the complex atomic structure of the multicomponent molten state. In this work, high-energy X-ray diffraction was used for analyzing the equiatomic multicomponent $Ti_{20}Zr_{20}Hf_{20}Cu_{20}Ni_{20}$ HE-MG. The short-to-medium-range orders (S-MROs) of the HE-MG were analyzed and

Hui-Qiang Ying and Si-Nan Liu contributed equally to this work.

H.-Q. Ying, S.-N. Liu, J.-C. Ge, H. Hahn, S. Lan*
School of Materials Science and Engineering, Herbert Gleiter Institute of Nanoscience, Nanjing University of Science and Technology, Nanjing 210094, China
e-mail: lansi@njust.edu.cn

Z.-D. Wu*
Center for Neutron Scattering and Applied Physics, City University of Hong Kong Dongguan Research Institute, Dongguan 523000, China
e-mail: zd.wu@cityu.edu.cn

W.-X. Dong, X.-L. Wang
Department of Physics, City University of Hong Kong, Hong Kong 999077, China

H. Hahn, V. Provenzano
Institute of Nanotechnology, Karlsruhe Institute of Technology (KIT), Eggenstein-Leopoldshafen 76344, Germany

compared with those of conventional MGs and crystalline HEAs. The short-range order (SRO) in this HE-MG resembles closely to that of a bcc crystalline structure. The medium-range order (MRO) in this HE-MG describes the arrangements of the bcc SRO structural motifs in three dimensions, is not of a single type and instead is observed to consist of different structural arrangements. In the crystallized state, the structural arrangement of the SRO structural motifs becomes more similar to that of the bcc crystalline structure. The role of the S-MRO in this phase selection is discussed in this paper.

In this work, the pre-alloyed ingots were prepared by melting Ti, Zr, Hf, Cu, Ni (purity $\geq$ 99.95 at%) raw material granules under a high-purity Ti-gettered argon atmosphere. The ingots were melted five times and flipped each time to improve the chemical homogeneity in a water-cooled copper crucible. After that, the $Ti_{20}Zr_{20}Hf_{20}Cu_{20}Ni_{20}$ glassy ribbons were prepared by single-roller melt-spinning. The thickness of the obtained ribbons is about 45 μm, and the width is 3 mm. XRD (Bruker-AXS D8 Advance) was used to check the amorphous states of the ribbons. The incident wavelength of the XRD is 0.154 nm, and the range of diffraction angle (2θ) is 20°–70°. The atomic structures were characterized using a JEM-F200 transmission electron microscope (TEM). From the amorphous ribbon, TEM samples with a diameter of 3 mm were punched and subsequently thinned by a twin-jet electropolishing using the electrolyte made of 8 vol% perchloric acid and 92 vol% methyl alcohol at a voltage of 25 V. The thermal properties were measured by differential scanning calorimetry (DSC, METTLER TOLEDO) in a high-purity N_2 atmosphere at a heating rate of 20 K·min^{-1}. High-energy X-ray diffraction measurements were performed at the beamline 11-ID-C of the advanced photon source (APS), Argonne National Laboratory. High-energy X-rays with a beam size of 500 μm × 500 μm and wavelength of 0.01173 nm were used for data collection. The structure factor $S(\boldsymbol{q})$ versus $\boldsymbol{q}$ was determined using PDFGETX2 [22], where $\boldsymbol{q}$ is the scattering vector. The reduced pair distribution function (PDF), $G(r)$, was obtained by Fourier transformation of $S(\boldsymbol{q})$, and the radial distribution functions $g(r)$ were calculated by $(G(r))/(4\pi r\rho_0) + 1$, where ρ_0 is the average number density, and r is the atomic distance.

Figure 1a shows the results of DSC for the as-prepared $Ti_{20}Zr_{20}Hf_{20}Cu_{20}Ni_{20}$ HE-MG ribbon, whereas the XRD pattern in the inset demonstrates the amorphous state. The onset temperatures of both the glass transition and the crystallization are denoted as T_g and T_x, respectively. Typically, in many metallic glasses, one or two prominent exothermic peaks in DSC curves have been found [23–25]. In contrast, in the present HE-MG, multiple exothermic peaks are found in the DSC curve at temperatures above T_g [26], indicating a complex crystallization behavior. Figure 1b shows the high-resolution TEM image of the $Ti_{20}Zr_{20}Hf_{20}Cu_{20}Ni_{20}$ HE-MG in the as-spun state, again confirming its amorphous structure. The DSC data suggest that the complex atomic structure of the HE-MG may induce a competition of different structural orders during the crystallization processes.

Figure 2 shows the high-energy X-ray diffraction of the $Ti_{20}Zr_{20}Hf_{20}Cu_{20}Ni_{20}$ HE-MG melt-spun ribbon. The inset in Fig. 2a is the structure factor ($S(\boldsymbol{q})$) derived from the scattering data by subtracting the background and correcting for absorption, multiple scattering, Compton scattering, etc. The $S(\boldsymbol{q})$ curve has a typical shape as other metallic glasses, in particular, no crystalline peaks are found. The $G(r)$ curve, as presented in Fig. 2a, shows multiple peaks representing the probability of finding the respective atoms at a certain distance. The atomic structure of the $Ti_{20}Zr_{20}Hf_{20}Cu_{20}Ni_{20}$ HE-MG displays a great topological and chemical complexity. In order to simplify the analysis of $G(r)$, the atomic species are divided into two groups, based on their chemical property and atomic radius. Table 1 summarizes the values of heat of mixing of the Ti, Zr, Hf, Cu, Ni elements. The atomic radii of these elements are found to be 0.147, 0.160, 0.159, 0.128, 0.124 nm, respectively. It shows that Ti, Zr, Hf have similar atomic radius and strong negative heat of mixing with Cu, Ni [27]. Thus, the elements Cu and Ni are treated as Group A, whereas the elements Ti, Zr, Hf are treated as Group B. Thus, the simplified $A_{40}B_{60}$ metallic glass (MG) is similar to the prototype $Cu_{40}Zr_{60}$ MG, reported extensively in the literature.

Compared to the published results for the $G(r)$ of Cu-Zr MGs [28], the $G(r)$ for the $Ti_{20}Zr_{20}Hf_{20}Cu_{20}Ni_{20}$ HE-MG (refer to Fig. 2a) displays a stronger splitting of the first peak, which is indicative of a stronger ordering. Figure 2b shows the enlarged view of the first peak of $G(r)$ in which the simplified atomic pairs are marked by the dashed line. It is observed that the A–A pairs, located at around 0.25 nm, make a negligible contribution to the first peak of $G(r)$. On the other hand, the A–B pairs, located between 0.27 and 0.285 nm, contribute to the first sub-peak (marked by the red arrow at 0.27 nm) of the first peak of $G(r)$. B–B pairs, located at 0.295 to 0.32 nm, contribute to the second sub-peak (marked by the red arrow at 0.313 nm) of the first peak.

To better understand the structural orders in the short to medium range, the radial distribution function, $g(r)$, for the HE-MG is plotted and shown in Fig. 3. Similar to the method used in work by Wu et al. [29], the $g(r)$ plot, presented in Fig. 3a, is scaled by the first peak position r_1. The relative atomic positions, scaled by the first peak positions of the face-centered cubic (fcc) and body-centered cubic (bcc) crystalline lattice structures, are also

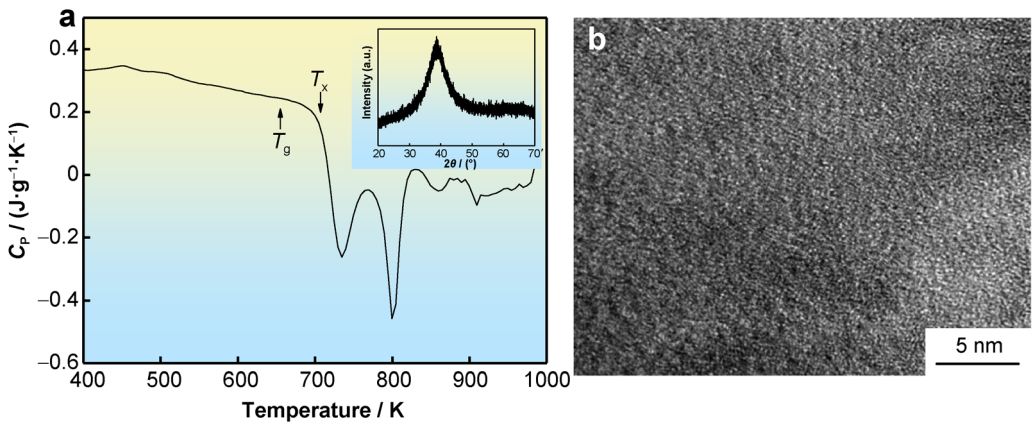

Fig. 1 **a** DSC curve of $Ti_{20}Zr_{20}Hf_{20}Cu_{20}Ni_{20}$ HE-MG melt-spun ribbon and (inset) XRD pattern; **b** high-resolution TEM image of $Ti_{20}Zr_{20}Hf_{20}Cu_{20}Ni_{20}$ HE-MG melt-spun ribbon

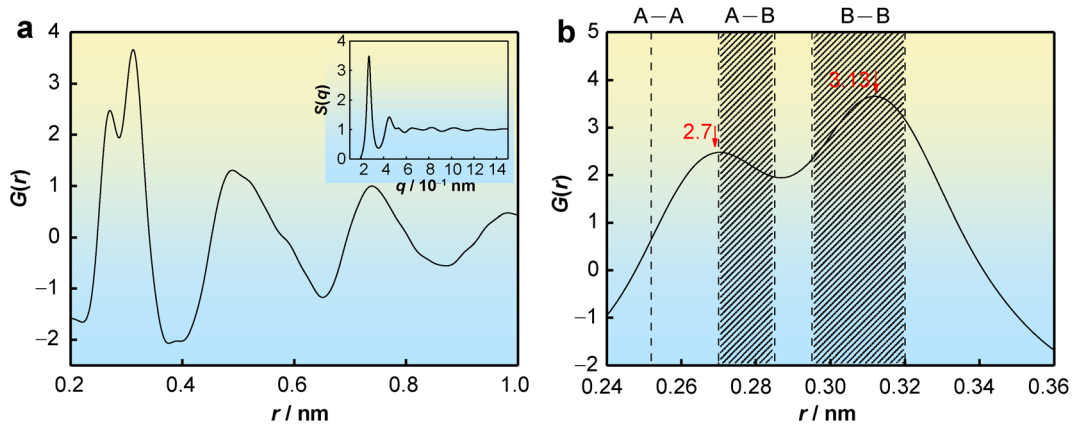

Fig. 2 **a** High-energy XRD results of as-spun $Ti_{20}Zr_{20}Hf_{20}Cu_{20}Ni_{20}$ HE-MG and (inset) $G(r)$ and $S(\boldsymbol{q})$ for HE-MG; **b** enlarged view of the first peak of $G(r)$ together with positions of atomic pairs, where A represents Ni and Cu and B represents Ti, Zr, Hf

Table 1 Values of heat of mixing (ΔH, kJ·mol ^{1}) between elements [27]

Elements	Ti	Zr	Hf	Cu	Ni
Ni	− 35	− 49	− 42	− 9	–
Cu	− 9	− 23	− 17	–	− 9
Hf	0	0	–	− 17	− 42
Zr	0	–	0	− 23	− 49
Ti	–	0	0	− 9	− 35

included in Fig. 3a. From the figure, it can be observed that for the first atomic shell, the SRO of the HE-MG closely resembles the bcc crystalline structure. By combining the results presented in Fig. 2 with those shown in Fig. 3, it can be seen that the Cu/Ni lies at the center of the bcc structure, whereas Ti/Zr/Hf lies at the vertex of the bcc structure. The second atomic shell also retains, to some degree, the bcc crystalline order, as three blue, dashed lines (representing the atomic positions of bcc lattice) lie around the second peak of $g(r/r_1)$ of the HE-MG. However, the peaks beyond the second atomic shell do not follow fcc or bcc crystalline order, but constitute broader peak width.

The $g(r)$ curve beyond the first atomic shell represents the atomic packing scheme at the medium range. The present results show that the atomic packing starts to deviate from bcc order at the second shell. Consequently, the second shell of $g(r)$ is fitted by four Gaussian peaks in Fig. 3b, with each peak representing 1-atom, 2-atom,

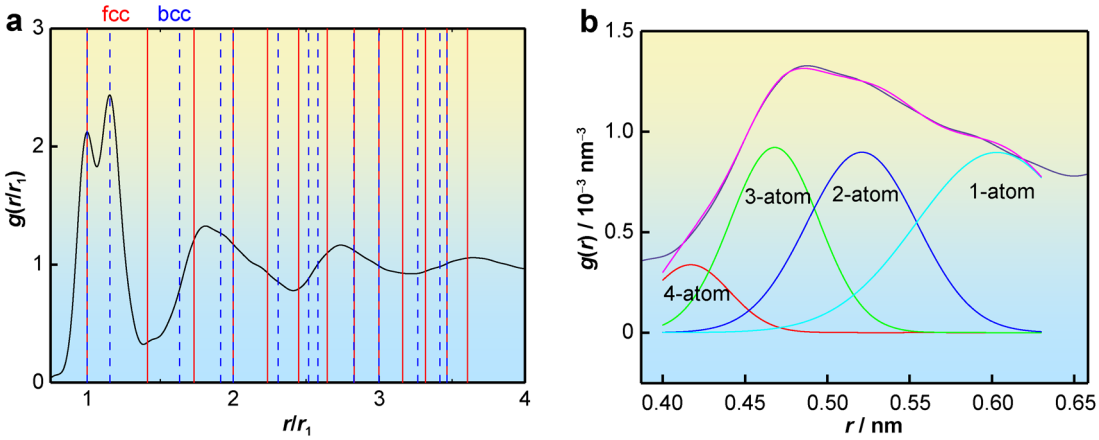

Fig. 3 **a** Scaled pair distribution function $g(r/r_1)$ of as-spun $Ti_{20}Zr_{20}Hf_{20}Cu_{20}Ni_{20}$ ribbon; **b** Gaussian fitting results of the second coordination shell in pair distribution functions $g(r)$

Table 2 Summary of proportion of different sharing modes of $Ti_{20}Zr_{20}Hf_{20}Cu_{20}Ni_{20}$ HE-MG and ideal bcc crystalline structure

Sharing mode	Proportion	
	$Ti_{20}Zr_{20}Hf_{20}Cu_{20}Ni_{20}$ HE-MG	Ideal bcc crystalline structure
1-atom	0.41	0.31
2-atom	0.28	0.46
3-atom	0.23	0.23
4-atom	0.08	0

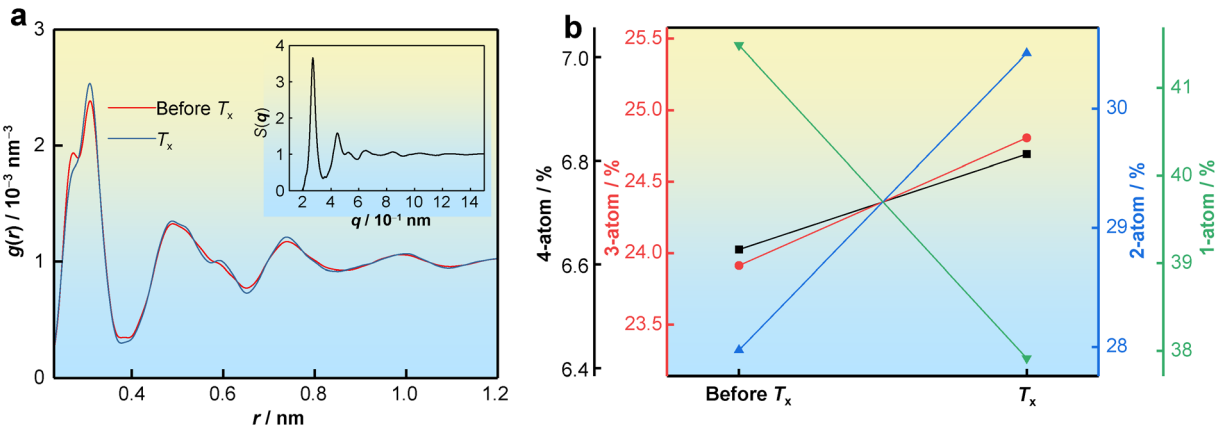

Fig. 4 **a** Pair distribution functions, $g(r)$, of sample before and after crystallization and (inset) $S(q)$ curve of crystallized sample; **b** percentage of four modes of cluster connectivity

3-atom and 4-atom sharing mode of the SRO clusters, respectively [30–33]. The proportion of each sharing scheme is summarized in Table 2. The connecting scheme of the SRO clusters in ideal bcc crystalline lattice and their proportions are also summarized in Table 2 for comparison. The sharing modes of the SRO clusters in the ideal bcc crystalline lattice include eight 1-atom sharing modes (vertex-shared), twelve 2-atom sharing modes (edge-shared), six 3-atom sharing modes (face-shared) and no 4-atom sharing modes (intercross-shared) [34], which produce three atom pairs in the second atomic shell marked by the dashed blue line (from 1.5 to 2 in r/r_1) in Fig. 3a. From Table 2, it can be observed that the connection of SRO clusters of the HE-MG has more 1-atom sharing

modes and less 2-atom sharing modes compared with bcc crystalline lattice. As the 1-atom sharing mode is vertex shared, its packing scheme is looser than that of the 2-atom sharing mode. Thus, the density of the HE-MG is expected to be lower than that of the bcc crystalline structure with the same chemical composition.

$g(r)$ curves, as shown in Fig. 4a, were also analyzed for samples heated both to a temperature just below the first crystallization temperature T_x and above T_x. The inset in Fig. 4a is the $S(\boldsymbol{q})$ curve of the sample heated above T_x, showing indications of initial crystallization. It is observed that after crystallization, the shoulder peaks at the nearest neighbor change their relative intensities, indicating an increase in B–B pairs accompanied by a decrease in A–B pairs. This most likely is the consequence of the local atomic rearrangements that requires detailed analysis including the use of molecular dynamics (MD) simulations, which will be performed in the future. Despite the changes in the shape of the first peak of $g(r)$, its peak positions remain unchanged, thus keeping the similarity to the bcc crystalline structure. Differences of the $g(r)$ curves at distances beyond the SRO were also found. This indicates that the MROs play an important role during the crystallization processes. The connecting schemes of the SRO clusters for samples before and after crystallization are obtained by fitting the second shell of the $g(r)$ curves, with the proportion of each mode being summarized in Fig. 4b. These results clearly show that after crystallization, the 1-atom sharing mode decreases abruptly and the 2-atom sharing mode increases abruptly, both converging to the value of bcc crystalline structure. On the other hand, the 3-atom sharing mode and 4-atom sharing mode remain nearly unchanged.

From the presented experimental results, it can be concluded that the $Ti_{20}Zr_{20}Hf_{20}Cu_{20}Ni_{20}$ HE-MG retains, to a certain degree, structural ordering at both the short- and medium-range scales. The S-MRO identified in the as-prepared HE-MG determines the evolution of the phases toward the crystalline structure. Here, it is recalled that the $Ti_{20}Zr_{20}Hf_{20}Cu_{20}Ni_{20}$ HE-MG is derived from a prototype metallic glass $Cu_{40}Zr_{60}$, and consequently, the SRO of the HE-MG is compared with that of the binary Cu-Zr MG. Antonowiczsupa et al. [35] found the dominant SRO in $Cu_{35}Zr_{65}$ was Cu-centered icosahedron by X-ray absorption fine structure method and molecular dynamics. Wang et al. [36] also found that icosahedron-like clusters were dominant in Cu-Zr BMGs. Mattern et al. [28] found that the local structures of $Cu_{35}Zr_{65}$ MG showed a large variety of polyhedra arrangements rather than a dominant type, by reverse Monte-Carlo method, high-energy X-ray and neutron diffraction. Peng et al. [37] showed that the SRO was composition-dependent, and the increase in Cu-content would result in an increase in icosahedron-like SRO in the Cu-Zr MG. However, the data presented both in Fig. 2 and Fig. 3 point out that the SRO of $Ti_{20}Zr_{20}Hf_{20}Cu_{20}Ni_{20}$ HE-MG resembles that of the bcc crystalline structure. This is not comparable to the reported icosahedron-like order in Cu-Zr MG, but coincides with the local order of the crystalline Ti-Zr-Hf HEA alloys [38].

Chen et al. [39] studied the atomic transport mechanism in an alloy of a similar composition, $Ti_{20}Zr_{20}Hf_{20}Cu_{20}Fe_{20}$, by quasielastic neutron scattering. Even in the liquid state, well above the melting temperature, the authors reported that groups of atoms having a length scale of about 2.1 nm diffused collectively. This would indicate a strong tendency to form MROs of the SRO cluster in the liquid state. The present $g(r)$ results also reveal the existence of MROs in the $Ti_{20}Zr_{20}Hf_{20}Cu_{20}Ni_{20}$ HE-MG. Additionally, the packing mode of MROs varies in the as-spun state and tends to the bcc crystalline structure at the onset of crystallization. In view of these observations, it is proposed that the packing and connection modes in the MRO regime determine the phase formation in the $Ti_{20}Zr_{20}Hf_{20}Cu_{20}Ni_{20}$ HE-MG. During quenching from the high-temperature molten state, the bcc-like SRO clusters lead to the formation of MRO with different connection modes. The packing schemes of the MRO gradually deviate from those of the bcc crystalline structure, as demonstrated by the $G(r)$ data. Finally, although the SRO is similar to bcc crystalline structure, a glass is formed because of the competition of different connection modes of the MROs, which introduces randomness in the structure, leading to an overall amorphous structure. On the contrary, in HEA systems forming crystalline structures, the bcc-like SRO transfers over larger distances, leading to more extended MRO, and consequently, to the formation of a crystalline solid solution. Similar results have been reported for a Pd-Ni-P bulk metallic glass [40], where the packing schemes of MROs determine the formation of either an amorphous structure or a crystalline cubic phase.

In summary, the present results show that in the $Ti_{20}Zr_{20}Hf_{20}Cu_{20}Ni_{20}$ HE-MG, the SRO inherits the bcc crystalline order of the crystalline Ti-Zr-Hf HEA series, while the MRO varies. On the other hand, after crystallization, the packing of MRO evolves to that of the bcc crystalline structure, with more edge-shared modes and less vertex-shared modes developed. It is suggested that the packing and connection of MROs frustrate the liquid structure and thus determine the evolution of either an amorphous structure or a crystalline solid solution. The present study helps to provide new physical insights regarding phase evolution and selection rules for the formation of HEAs and HE-MGs.

Acknowledgements This work was financially supported by the National Key R&D Program of China (No. 2021YFB3802800), the

National Natural Science Foundation of China (Nos. 51871120 and 51571170), the Fundamental Research Funds for the Central Universities (Nos. 30919011107 and 30919011404), the Natural Science Foundation of Jiangsu Province (No. BK20200019) and Shenzhen Fundamental Research Program (No. JCYJ20200109105618137). Z.-D. Wu and S. Lan acknowledge the support by Guangdong-Hong Kong-Macao Joint Laboratory for Neutron Scattering Science and Technology. X.-L. Wang acknowledges the support by Shenzhen Science and Technology Innovation Committee (No. JCYJ20170413140446951) and the Ministry of Science and Technology of China (No. 2016YFA0401501). H. Hahn acknowledges the financial support of the Deutsche Forschungsgemeinschaft (No.HA 1344/46-1). This research used the resources of the Advanced Photon Source, a US Department of Energy (DOE) Office of Science User Facility operated for the DOE Office of Science by Argonne National Laboratory (No. DE-AC02-06CH11357).

Declarations

Conflicts of interests The authors declare that they have no conflicts of interests.

References

[1] Naeem M, He HY, Zhang F, Huang HL, Harjo S, Kawasaki T, Wang B, Lan S, Wu ZD, Wang F, Wu Y, Lu ZP, Zhang ZW, Liu CT, Wang XL. Cooperative deformation in high-entropy alloys at ultralow temperatures. Science Advances. 2020;6(13):4002.

[2] Gludovatz B, Hohenwarter A, Catoor D, Chang EH, George EP, Ritchie RO. A fracture-resistant high-entropy alloy for cryogenic applications. Science. 2014;345(6201):1153.

[3] Shi PJ, Ren WL, Zheng TX, Ren ZM, Hou XL, Peng JC, Hu PF, Gao YF, Zhong YB, Liaw PK. Enhanced strength-ductility synergy in ultrafinegrained eutectic high-entropy alloys by inheriting microstructural lamellae. Nature Communications. 2019;10(1):489.

[4] He HY, Naeem M, Zhang F, Yi Lu Zhao, Harjo S, Kawasaki T, Wang B, Wu XL, Lan S, Wu ZD, Wu Y, Lu ZP, Kai JJ, Liu CT, Wang XL. Stacking fault driven phase transformation in CrCoNi medium entropy alloy. Nano Letters. 2021;21(3):1419.

[5] Niu SZ, Kou HC, Wang J, Li JS. Improved tensile properties of $Al_{0.5}$CoCrFeNi high-entropy alloy by tailoring microstructures. Rare Metals. 2021;40(9):2508.

[6] Zhang Y, Zuo TT, Tang Z, Gao MC, Dahmen KA, Liaw PK, Lu ZP. Microstructures and properties of high-entropy alloys. Progress in Materials Science. 2014;61:1.

[7] Xian X, Zhong ZH, Lin LJ, Zhu ZX, Chen C, Wu YC. Tailoring strength and ductility of high-entropy CrMnFeCoNi alloy by adding Al. Rare Metals. 2018; https://doi.org/10.1007/s12598-018-1161-4.

[8] Hu YM, Liu XD, Guo NN, Wang L, Su YQ, Guo JJ. Microstructure and mechanical properties of NbZrTi and NbHfZrTi alloys. Rare Metals. 2019;38(9):840.

[9] Qin YC, Wang FQ, Wang XM, Wang MW, Zhang WL, An WK, Wang XP, Ren YL, Zheng X, Lu DC. Noble metal-based high-entropy alloys as advanced electrocatalysts for energy conversion. Rare Metals. 2021;40(9):2354.

[10] Feng CS, Lu TW, Wang TL, Lin MZ, Hou J, Lu W, Liao WB. A novel high-entropy amorphous thin film with high electrical resistivity and outstanding corrosion resistance. Acta Metallurgica Sinica(English Letters). 2021;34(11):1537.

[11] Chen Y, Dai ZW, Jiang JZ. High entropy metallic glasses: glass formation, crystallization and properties. Journal of Alloys and Compounds. 2021;866(23):158852.

[12] Gong P, Yin G, Jamili-Shirvan Z, Ding HY, Wang XY, Jin JS. Influence of deep cryogenic cycling on the rejuvenation and plasticization of TiZrHfBeCu high-entropy bulk metallic glass. Materials Science & Engineering A. 2020; 797:140078.

[13] Li CZ, Li Q, Li MC, Chang CT, Li HX, Dong YQ, Sun YF. New ferromagnetic $(Fe_{1/3}Co_{1/3}Ni_{1/3})_{80}(P_{1/2}B_{1/2})_{20}$ high entropy bulk metallic glass with superior magnetic and mechanical properties. Journal of Alloys & Compounds. 2019;791(1):947.

[14] Zhang SY, Gao YY, Zhang ZB, Gu T, Liang XB, Wang LZ. Research progress on functional properties of novel high-entropy metallic-glasses. Chinese Journal of Rare Metals. 2021; 45(6):717

[15] Ji LL, Yun XB, Lü YZ. Preparation of $Zr_{50}Ti_5Cu_{27}Ni_{10}Al_8$ bulk amorphous alloy by spark plasma sintering. Chinese Journal of Rare Metals. 2020;44(11):1221

[16] Zhao SF, Yang GN, Ding HY, Yao KF. A quinary Ti–Zr–Hf–Be–Cu high entropy bulk metallic glass with a critical size of 12 mm. Intermetallics. 2015;61(1):47.

[17] Liu Y, Wang HJ, Pang SJ, Zhang T. Ti–Zr–Cu–Fe–Sn–Si–Ag–Ta bulk metallic glasses with good corrosion resistance as potential biomaterials. Rare Metals. 2020;39(6):688.

[18] Wang XF, Zhang Y, Qiao Y, Chen GL. Novel microstructure and properties of multicomponent CoCrCuFeNiTi$_x$ alloys. Intermetallics 2007;15(3):357.

[19] Chen MR, Lin SJ, Yeh JW, Chen SK, Huang YS, Tu CP. Microstructure and properties of $Al_{0.5}$CoCrCuFeNiTi$_x$ (x=0–2.0) highentropy alloys. Materials Transactions. 2006;47(5):1395.

[20] Guo S, Liu CT. Phase stability in high entropy alloys: formation of solid-solution phase or amorphous phase. Progress in Natural Science: Materials International. 2011;21(6):433.

[21] Yang X, Zhang Y. Prediction of high-entropy stabilized solid-solution in multi-component alloys - ScienceDirect. Materials Chemistry and Physics. 2012;132(2–3):233.

[22] Lan S, Ren Y, Wei XY, Wang B, Gilbert EP, Shibayama T, Watanabe S, Ohnuma M, Wang XL. Hidden amorphous phase and reentrant supercooled liquid in Pd-Ni-P metallic glasses. Nature Communications. 2017;8(1):14679.

[23] Kui HW, Greer AL, Turnbull D. Formation of bulk metallic glass by fluxing. Applied Physics Letters. 1984;45(6):615.

[24] Peker A, Johnson WL. A highly processable metallic glass: $Zr_{41.2}Ti_{13.8}Cu_{12.5}Ni_{10.0}Be_{22.5}$. Applied Physics Letters. 1993;63(17): 2342.

[25] Inoue A. Stabilization of metallic supercooled liquid and bulk amorphous alloys. Acta Materialia. 2000;48(1):279.

[26] Ma LQ, Wang LM, Zhang T, Inoue A. Bulk glass formation of Ti-Zr-Hf-Cu-M (M=Fe, Co, Ni) alloys. Materials Transactions. 2002;43(2):277.

[27] Takeuchi A, Inoue A. Classification of bulk metallic glasses by atomic size difference, heat of mixing and period of constituent elements and its application to characterization of the main alloying element. materials transactions. 2005;46(12):2817.

[28] Mattern N, Jóvári P, Kaban I, Gruner S, Elsner A, Kokotin V, Franz H, Beuneu B, Eckert J. Short-range order of Cu–Zr metallic glasses. Journal of Alloys & Compounds. 2009; 485(1-2):163.

[29] Wu ZW, Li MZ, Wang WH, Liu KX. Hidden topological order and its correlation with glass-forming ability in metallic glasses. Nature communications. 2015;1(6):6035.

[30] Liu SN, Wang LF, Ge JC, Wu ZD, Ke YB, Li Q, Sun BA, Feng T, Wu Y, Wang JT, Hahn H, Ren Y, Almer JD, Wang XL, Lan S. Deformationenhanced hierarchical multiscale structure heterogeneity in a Pd-Si bulk metallic glass. Acta Materialia. 2020;200:42.

[31] Ding J, Ma E. Computational modeling sheds light on structural evolution in metallic glasses and supercooled liquids. Npj Computational Mathematics. 2017;3(1):9.

[32] Pan SP, Qin JY, Wang WM, Gu TK. Origin of splitting of the second peak in the pair-distribution function for metallic glasses. Physical Review B. 2011;84(9):92201.

[33] Du JL, Wen B. Composition-structure-property correlations of complex metallic alloys described by the "cluster-plus-glue-atom" model. Applied Materials Today. 2017;7:13.

[34] Li F, Liu XJ, Lu ZP. Atomic structural evolution during glass formation of a Cu–Zr binary metallic glass. Computational Materials Science. 2014;85:147.

[35] Antonowiczsupa J, Pietnoczkasupa A, Drobiazgsupa T, Almyrassupb GA, Papageorgiousupc DG, Evangelakissupc GA. Icosahedral order in Cu-Zr amorphous alloys studied by means of X-ray absorption fine structure and molecular dynamics simulations. Philosophical Magazine. 2012;92(15):1865.

[36] Wang XD, Yin S, Cao QP, Jiang JZ, Franz H, Jin ZH. Atomic structure of binary $Cu_{64.5}Zr_{35.5}$ bulk metallic glass. Applied Physics Letters. 2008;92(1):1531.

[37] Peng HL, Li MZ, Wang WH, Wang CZ, Ho KM. Effect of local structures and atomic packing on glass forming ability in Cu_xZr_{100-x} metallic glasses. Applied Physicsletters. 2010;96(2): 021901.1.

[38] Yuan Y, Wu Y, Yang Z, Liang X, Lei ZF, Huang HL, Wang H, LiuXJ, An K, Wu W. Formation, structure and properties of biocompatible TiZrHfNbTa high-entropy alloys. Materials Research Letters. 2019;7(6):225.

[39] Chen CJ, Wong K, Krishnan RP, Lei ZF, Yu DH, Lu ZP, Chathoth SM. Highly collective atomic transport mechanism in high-entropy glassforming metallic liquids. Journal of Materials Science & Technology. 2019;35(1):44.

[40] Lan S, Zhu L, Wu ZD, Gu L, Zhang QH, Kong HH, Liu JZ, Song RY, Liu SN, Sha G, Wang YG, Liu Q, Liu W, Wang PY, Liu CT, Ren Y, Wang XL. A medium-range structure motif linking amorphous and crystalline states. Nature Materials. 2021;20(10):1347.